Article

Giant and controllable nonlinear magneto-optical effects in two-dimensional magnets

Check for updates

Dezhao Wu [1], Meng Ye [2] ✉, Haowei Chen[1], Yong Xu [1,3,4] ✉ & Wenhui Duan [1,3,5]

The interplay of polarization and magnetism in materials with light can create rich nonlinear magneto-optical (NLMO) effects, and the recent discovery of two-dimensional (2D) van der Waals magnets provides remarkable control over NLMO effects due to their superb tunability. Here, based on first-principles calculations, we reported giant NLMO effects in CrI$_3$-based 2D magnets, including a dramatic change of second-harmonics generation (SHG) polarization direction (90°) and intensity (on/off switch) under magnetization reversal and a 100% SHG circular dichroism effect. We further revealed that these effects could not only be used to design ultra-thin multifunctional optical devices but also to detect subtle magnetic orderings. Remarkably, we analytically derived conditions to achieve giant NLMO effects and proposed general strategies to realize them in 2D magnets. Our work not only uncovers a series of intriguing NLMO phenomena but also paves the way for both fundamental research and device applications of ultra-thin NLMO materials.

The interaction of light with polarization and magnetization in matters could create profound nonlinear magneto-optical (NLMO) phenomena, such as the magnetization-induced second-harmonics generation (MSHG) and the photocurrent generation[1–3]. Among them, NLMO effects related to second-harmonics generation (SHG) have distinctive advantages in both magnetization detection and light modulation. As an all-optical probe characterized by higher-rank tensors, SHG-related NLMO measurement is nondestructive with high spatial and temporal resolution[4–8] and shows great promise to characterize structural and magnetic signals in 2D magnets[9–11]. Moreover, the rotation angle of the SHG-related NLMO effect is independent of sample thickness[12], which is in clear contrast to the thickness-dependent linear magneto-optical Faraday angle and, therefore, has the potential to be used in miniature devices.

The most significant SHG signal originates from electric dipole transitions[8], in which the breaking of the inversion ($\mathcal{P}$) symmetry is necessary. $\mathcal{P}$ symmetry can be broken by either crystal or magnetic structures, generating the corresponding crystal SHG and MSHG. These two types of SHG are described by an i-type tensor χ_N, which has even-parity under time-reversal ($\mathcal{T}$) operation, and a c-type tensor χ_M, which is $\mathcal{T}$-odd[13–17], respectively. Therefore, in non-centrosymmetric materials with $\mathcal{T}$ symmetry, only χ_N survives, and in non-centrosymmetric magnetic

materials with space-time inversion ($\mathcal{PT}$) symmetry, only χ_M survives (Detailed derivations are in Supplementary Note 1A). When both types of SHG coexist, that is, in materials with the simultaneous breaking of $\mathcal{P}$, $\mathcal{T}$ and $\mathcal{PT}$ symmetries, a class of specific NLMO effects arises due to the interference of χ_N and χ_M under $\mathcal{T}$-operation as

$$\mathbf{P}(2\omega) \propto (\chi_\mathrm{N} \pm \chi_\mathrm{M})\mathbf{E}(\omega)\mathbf{E}(\omega), \qquad (1)$$

where $\mathbf{E}(\omega)$ is the electric field of the incident light and $\mathbf{P}(2\omega)$ is the nonlinear polarization. The $\pm$ represents the influence of $\mathcal{T}$-operation. We denoted this interference effect of χ_N and χ_M as the NLMO effect in the rest of the context. As illustrated in Fig. 1, The interference between the two types of SHG can change the intensity of second harmonic (SH) light through $I(2\omega) \propto |\mathbf{P}(2\omega)|^2 \propto |\chi_\mathrm{N} \pm \chi_\mathrm{M}|^2$. Thus, in magnets with comparable crystal SHG and MSHG, notable NLMO effects can emerge.

However, experimentally observed NLMO effects in bulk materials are usually small[6,12,18–23], which seriously hinders the relevant research and applications of these effects. Additionally, a more profound theoretical understanding to explain and control the magnitude of NLMO effects is also absent. In contrast to bulk materials, recent experiments reveal many unusual SHG responses in two-dimensional (2D) materials, such as the

---

[1]State Key Laboratory of Low Dimensional Quantum Physics and Department of Physics, Tsinghua University, 100084 Beijing, China. [2]Graduate School of China Academy of Engineering Physics, 100193 Beijing, China. [3]Frontier Science Center for Quantum Information, Beijing, China. [4]RIKEN Center for Emergent Matter Science (CEMS), Wako, Saitama 351-0198, Japan. [5]Institute for Advanced Study, Tsinghua University, 100084 Beijing, China. ✉e-mail: mye@gscaep.ac.cn; yongxu@mail.tsinghua.edu.cn

1

large and tunable i-type SHG in MoS_2[24,25], $NbOI_2/Cl_2$ layers[26,27] and twisted h-BN[28,29], the giant pure c-type SHG in $\mathcal{PT}$-symmetric ultrathin CrI_3[1], $MnPS_3$[30] and $CrSBr$[31], and the anomalous SHG of uncertain origin in $MnBi_2Te_4$ thin films[32] and monolayer (ML) NiI_2[33]. These inspiring advances, combined with the great tunability of atomically thin materials, made 2D materials an excellent platform for both fundamental research and the design of miniature devices based on NLMO effects.

In this work, based on the computational method developed in refs. 34,35 and symmetry analysis, we investigated the NLMO effects of representative 2D magnets possessing both χ_N and χ_M, including trilayer ABA stacking CrI_3, ML Janus $Cr_2I_3Br_3$, and ML H-VSe_2. We analytically derived and numerically calculated the NLMO angle for linearly polarized incident light and the NLMO intensity asymmetry for circularly polarized incident

light at different frequencies. Remarkably, we uncovered giant NLMO effects due to the maximal interference between comparable χ_N and χ_M in CrI_3-based 2D magnets, including a nearly 90° polarization rotation or an on/off switching of certain light helicity of SH light upon magnetization reversal and a maximal SHG circular dichroism (SHG-CD) effect within fixed magnetization. We also found that these NLMO effects are extremely sensitive to subtle changes in complex magnetic orders. Moreover, we revealed the influence of interlayer interaction, spin-orbit coupling (SOC), and synergistic effect of stacking and magnetic orders to NLMO effects and proposed strategies to achieve these giant NLMO effects in more 2D materials. Our work not only uncovered a series of giant NLMO effects and corresponding candidate materials but also provides strategies to manipulate these effects in other material systems, and further shed light on the application of NLMO effects in subtle magnetic orders detection and ultrathin optical devices.

Results and discussion
Structures and SHG of representative 2D magnets
NLMO effects exist in magnetic materials without $\mathcal{PT}$ symmetry and therefore, we considered two typical ferromagnetic (FM) semiconductors in the monolayer limit, CrI_3 and H-VSe_2[36–42]. ML VSe_2 is non-centrosymmetric with magnetic symmetry $\bar{6}m'2'$ when the magnetization is along the $\hat{z}$ axis. ML CrI_3 is centrosymmetric with magnetic symmetry $\bar{3}m'$[43] and AB stacking bilayer CrI_3 has $\mathcal{PT}$ symmetry as shown in Supplementary Fig. 2; therefore, the ML does not have SHG, and the bilayer only has the MSHG χ_M. In the following, we used the strategy of multi-layer stacking and element replacement to break $\mathcal{P}$ and $\mathcal{PT}$ to enable NLMO effects in CrI_3-related materials. The simplest examples are ABA stacking trilayer CrI_3 with antiferromagnetic (AFM) interlayer coupling (denoted by ABA-AFM CrI_3) and ML Janus $Cr_2I_3Br_3$. Figure 2a, c, e shows the atomic and magnetic structures of ABA-AFM CrI_3, ML $Cr_2I_3Br_3$, and ML H-VSe_2
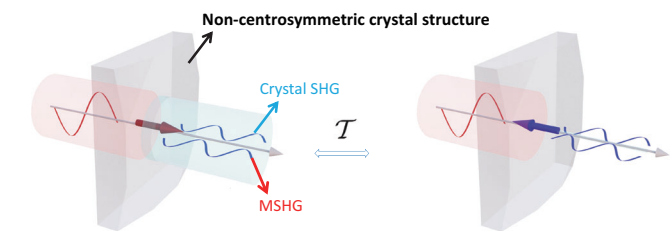
Fig. 1 | Concept of NLMO effects. Magnets with non-centrosymmetric crystal structures exhibit both the crystal SHG and the MSHG due to the simultaneous breaking of $\mathcal{P}$, $\mathcal{T}$ and $\mathcal{PT}$ symmetries. The crystal SHG is unaffected by the magnetization direction reversal while the MSHG changes the sign. Thus, the two terms can constructively (left panel) or destructively (right panel) interfere with each other for the positive and negative magnetization directions, respectively, which leads to NLMO effects. The red and blue arrows represent magnetic orders related by $\mathcal{T}$ operation.
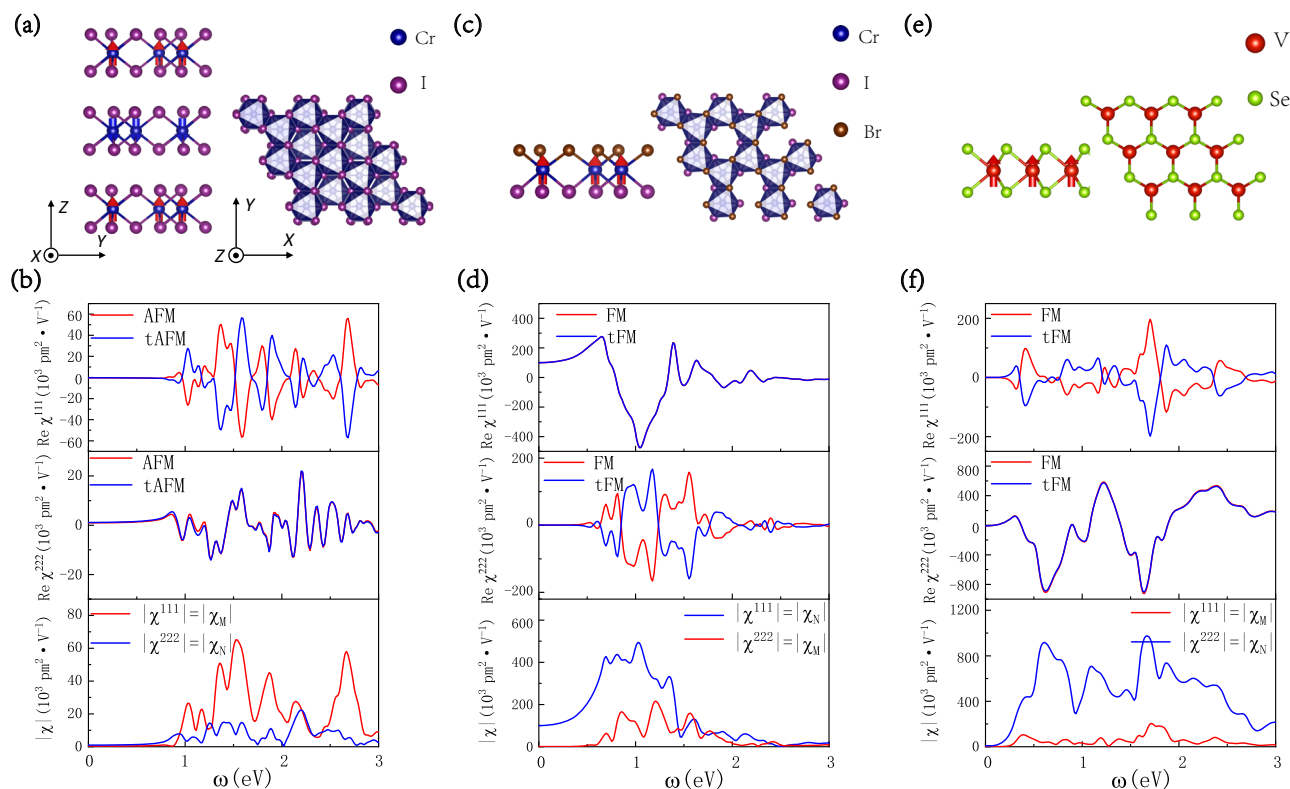
Fig. 2 | Atomic structures and SHG of the representative 2D magnets. a, c, e Top and side views of ABA CrI_3 with AFM (↑↓↑) magnetic order, ML $Cr_2I_3Br_3$ and ML H-VSe_2 with FM (↑) magnetic order. The red/blue arrows represent the magnetic moment of each atom. **b, d, f** The real parts and the norm of SHG susceptibility tensor components. The red and blue lines represent the results of AFM (↑↓↑)/FM (↑) orders and their $\mathcal{T}$-related tAFM (↓↑↓)/tFM (↓) orders, respectively.

Table 1 | Magnetic symmetries and symmetry properties of SHG tensor components of representative 2D magnets

	AB-AFM CrI$_3$		ABA-AFM CrI$_3$	ML Cr$_2$I$_3$Br$_3$	ML H-VSe$_2$	ABA-MIX CrI$_3$
Magnetic point group	$\bar{3}$		$32'$	$3m'$	$\bar{6}m'2'$	3
χ_N	NA		$222 = -211 = -112$	$111 = -122 = -212$	$222 = -211 = -112$	$111 = -122 = -212$ and $222 = -211 = -112$
χ_M	$111 = -122 = -212$ and $222 = -211 = -112$		$111 = -122 = -212$	$222 = -211 = -112$	$111 = -122 = -212$	$111 = -122 = -212$ and $222 = -211 = -112$

χ_N and χ_M represent the $\mathcal{T}$-even and $\mathcal{T}$-odd SHG components. If a tensor component has both χ_N and χ_M parts, it means this tensor component does not have a definite parity under $\mathcal{T}$.

with their magnetic symmetries summarized in Table 1. Their band structures are shown in Supplementary Note 5.

Figure 2b, d, f shows the influence of $\mathcal{T}$ operation to different SHG components $\chi^{abc}(2\omega; \omega, \omega)$ of the above mentioned materials. In the rest of the article, we used the shorthand notation χ^{abc} to represent $\chi^{abc}(2\omega; \omega, \omega)$, where a, b, c are Cartesian directions. The two magnetic orders related by $\mathcal{T}$ symmetry are denoted as AFM/FM and tAFM/tFM, respectively. For SHG susceptibilities of trilayer CrI$_3$, we scissored the band gap to 1.5 eV, and our results show good agreement with the previous work[43] (Supplementary Fig. 3). Due to the C_{3z} symmetry in all three representative materials, each material has only two independent in-plane SHG components, that is $\chi^{111} = -\chi^{122} = -\chi^{212}$ and $\chi^{222} = -\chi^{211} = -\chi^{112}$, where the subscripts 1 and 2 denote the Cartesian direction $\hat{x}$ and $\hat{y}$. Due to the presence of m' or $2'$ symmetry in all three materials, one of the SHG components is $\mathcal{T}$-odd while the other is $\mathcal{T}$-even, as shown in the upper and middle panels of Fig. 2b, d, f. Generally, the even and odd quantities can coexist in the same tensor component, and in this case, $\chi_N = (\chi + \mathcal{T}\chi)/2$, and $\chi_M = (\chi - \mathcal{T}\chi)/2$, where $\mathcal{T}\chi$ is the SHG susceptibility of the time-reversal pair. The detailed expressions of χ_N and χ_M, as well as their symmetry requirements, are summarized in Supplementary Note 1. The parity of each component under $\mathcal{T}$ is also summarized in Table 1.

The bottom panel of Fig. 2b, d, f clearly shows that the relative values of $|\chi_N|$ and $|\chi_M|$ are distinctive in the three materials. Although $|\chi_M|$ exceeds $|\chi_N|$ in ABA-AFM CrI$_3$ at a wide frequency range and the opposite is observed in ML Cr$_2$I$_3$Br$_3$, there are still several intersections of $|\chi_N|$ and $|\chi_M|$. In contrast, $|\chi_N|$ is much larger than $|\chi_M|$ in ML H-VSe$_2$ without any intersections.

Giant NLMO effects of representative 2D magnets

The coexistence of χ_N and χ_M can induce a variety of NLMO effects. In the following, we calculated the SHG responses under the linearly and the circularly polarized light (LPL and CPL), with an emphasis on the role of different ratios of χ_N and χ_M to NLMO effects. Considering a normal incidence geometry where the material is in the xy-plane and the incident light propagates in the $-\hat{z}$ direction, the SHG polarization $\mathbf{P}(2\omega)$ of 2D materials has been given in ref. 43. As the intensity of the emitted SH light $I(2\omega)$ is proportional to $|\mathbf{P}(2\omega)|^2$ and is commonly measured, we calculated $|\mathbf{P}(2\omega)|^2$ to represent $I(2\omega)$.

For LPL characterized by $\mathbf{E} = E(\cos\theta, \sin\theta)$, where θ denotes the angle between light polarization and the x-axis of the sample, we investigated the polarization-resolved SHG as a function of θ. The experiment measures the parallel ($\parallel$) and perpendicular ($\perp$) components of the SHG signal with respect to the direction of the incoming light polarization while the sample rotates with the angle θ. In the three representative materials, the SHG intensity at the parallel and perpendicular polarization directions can be written as[43]

$$I_\parallel(\theta) \propto |\chi^{111}\cos 3\theta - \chi^{222}\sin 3\theta|^2 E^4,$$
$$I_\perp(\theta) \propto |\chi^{111}\sin 3\theta + \chi^{222}\cos 3\theta|^2 E^4. \quad (2)$$

Both the parallel and perpendicular components exhibit sixfold sunflower-like patterns and differ only by a $\pm\pi/6$ angle, as the black and red lines shown in Fig. 3b. In addition, the angle θ_m corresponding to the maximum (minimum) of $I_\parallel$ also corresponds to the minimum (maximum) of $I_\perp$.

NLMO effects under LPL are reflected by comparing the polarization-resolved SHG patterns before and after $\mathcal{T}$ operation, which results from the sign reversal of χ_M. Under the symmetry of the three representative materials, this corresponds to a rotation of the polarization-resolved SHG pattern (Supplementary Figs. 5b and 7b), denoted as NLMO angle $\theta_\mathcal{T}$ (see details in Supplementary Note 2A), with the expression

$$\theta_\mathcal{T} = 2\theta_m = -\frac{\tan^{-1}\left(\tan 2\delta \cos \Delta\varphi\right)}{3} + \frac{n\pi}{3}, \quad (3)$$

where n is an integer originated from the rotation symmetry of the pattern. $\tan\delta = \frac{|\chi^{111}|}{|\chi^{222}|} \in (0, +\infty)$ is the magnitude ratio of χ^{111} and χ^{222}, and $\Delta\varphi = -i\left(\ln\frac{\chi^{111}}{|\chi^{111}|} - \ln\frac{\chi^{222}}{|\chi^{222}|}\right) \in (-\pi, +\pi]$ is the phase difference between χ^{111} and χ^{222}. The range of δ is $(0, \pi/2)$. Eq. (3) does not hold when $|\chi^{111}| = |\chi^{222}|$ and $\Delta\varphi = \pm \pi/2$. In this situation, the polarization-resolved SHG is isotropic according to Eq. (2), therefore, it does not show any change under $\mathcal{T}$ operation.

The maximum NLMO angle can be achieved is $\theta_\mathcal{T} = \pi/6 + n\pi/3$ with the condition

$$\begin{cases} |\chi^{111}| = |\chi^{222}|, \\ \Delta\varphi \neq \pm \pi/2, \end{cases} \quad (4)$$

and we denoted the corresponding frequency as the LPL characteristic frequency ω_{LPL}. At ω_{LPL}, the patterns of $I_\parallel$ and $I_\perp$ are swapped exactly, as shown in Fig. 3b, which results in a remarkable polarization change of the SH light. If the magnitude of $I_\parallel$ and $I_\perp$ differs greatly, the polarization of the SH light can rotate nearly $\pi/2$ under $\mathcal{T}$. The condition to achieve the $\pi/2$ polarization rotation at $\theta_m = \pi/12 + n\pi/6$ is

$$\begin{cases} |\chi^{111}| = |\chi^{222}|, \\ \Delta\varphi = 0 \text{ or } \pi, \end{cases} \quad (5)$$

and the corresponding frequency is denoted as ω'_{LPL}, which is a subset of ω_{LPL}. This condition is also graphically shown in the complex plane in Supplementary Fig. 1.

We numerically traced the ω-dependence of the NLMO angle $\theta_\mathcal{T}$ in the three representative materials, as shown in Fig. 3a. As highlighted by the dashed horizontal line, $\theta_\mathcal{T}$ close to $\pi/6 + n\pi/3$ corresponds to the largest NLMO angle. Remarkably, $\theta_\mathcal{T}$ is giant in ABA-AFM CrI$_3$ and ML Cr$_2$I$_3$Br$_3$ at several ω_{LPL} frequencies. In contrast, $\theta_\mathcal{T}$ is always tiny in ML H-VSe$_2$. This distinction is consistent with their different ratio of $|\chi_N|$ and $|\chi_M|$ susceptibilities observed in Fig. 2b, d, f. Figure 3b shows the dramatic change of SHG light from perpendicular to parallel polarization direction for incident light at $\theta_m = \pi/12$ (indicated by the yellow line) under $\mathcal{T}$ in this atomically thin Cr$_2$I$_3$Br$_3$ at $\omega'_{LPL} = 1.71$ eV.

Next, we investigated the polarization and intensity of SH light under the illumination of the CPL. For the CPL characterized by $\mathbf{E} = E(1, \pm i)$, where $\pm$ represents the left/right-handed ($\sigma^\pm$) CPL, the polarization of the SHG signal is

$$\mathbf{P}(2\omega) = 2E^2(\chi^{111} \mp i\chi^{222})(1, \mp i) \quad (6)$$
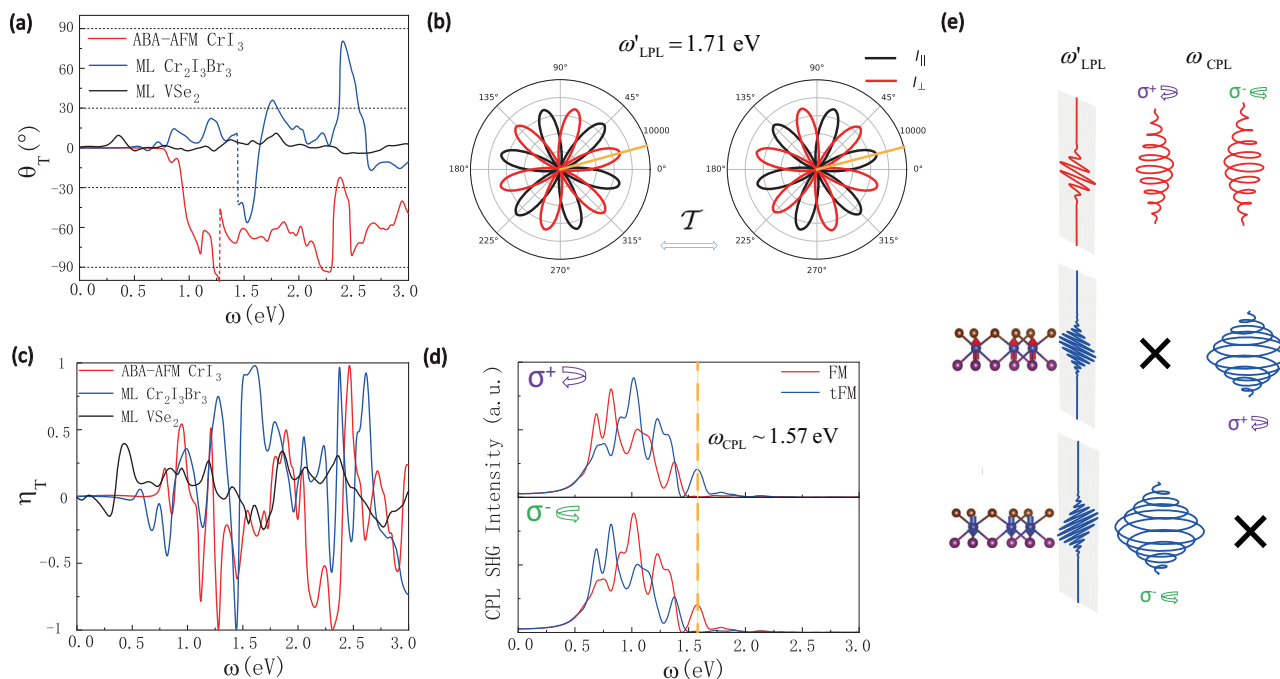
Fig. 3 | NLMO effects in representative 2D magnets. a The NLMO angle and **c** NLMO intensity asymmetry as a function of frequency. The vertical dashed lines in the curves indicate the NLMO rotation is ill-defined at the corresponding frequencies, and the polarization-resolved SHG close to those frequencies in ABA-CrI$_3$ and ML Cr$_2$I$_3$Br$_3$ are shown in Supplementary Figs. 5a and 7a. **b** Change of polarization-resolved SHG under $\mathcal{T}$ operation at a LPL characteristic frequency $\omega'_{LPL} = 1.71$ eV of ML Cr$_2$I$_3$Br$_3$. The yellow line marks one of the LPL incident angles where the maximal polarization direction change of SHG happens under $\mathcal{T}$ operation. **d** CPL SHG intensity of FM and tFM states of ML Cr$_2$I$_3$Br$_3$. The upper and lower panels are for incident helicity σ^+ and σ^-. The difference between the red

and blue curves in each panel reflects the NLMO intensity asymmetry. For a particular magnetic order, the difference between the upper and lower panels reflects the magnitude of SHG-CD. The dashed yellow line indicates one of the CPL characteristic frequencies $\omega_{CPL} = 1.57$ eV of ML Cr$_2$I$_3$Br$_3$. **e** Multi-degree controlling of NLMO in ML Cr$_2$I$_3$Br$_3$. For linearly-polarized incident light at polarization angle $\theta = \pi/12 + n\pi/6$ and frequency ω'_{LPL}, ML Cr$_2$I$_3$Br$_3$ can act as a magneto-optical polarization switcher. For circularly polarized incident light at frequency ω_{CPL}, ML Cr$_2$I$_3$Br$_3$ can act as a magneto-optical switch for circularly polarized SH light or an optical filter for circularly polarized SH light with a particular helicity.

according to Table 1. The SH light is also CPL with helicity opposite to the incident light. Furthermore, the intensity of the SH light depends on the helicity of the incident light, which is called the SHG-CD effect[44–46]. The SHG-CD intensity asymmetry can be described by

$$\eta_h^{\mathbf{M}} = \frac{I^+(\mathbf{M}) - I^-(\mathbf{M})}{I^+(\mathbf{M}) + I^-(\mathbf{M})}, \qquad (7)$$

where $I^+(\mathbf{M})$ is the SHG intensity generated by the magnetic order $\mathbf{M}$ when the helicity of the incident light is σ^+.

$\mathcal{T}$ operation can also change the intensity of the SH light with a certain helicity. We can define the NLMO intensity asymmetry at certain incident light helicity σ as

$$\eta_{\mathcal{T}}^{\sigma} = \frac{I^\sigma(+\mathbf{M}) - I^\sigma(-\mathbf{M})}{I^\sigma(+\mathbf{M}) + I^\sigma(-\mathbf{M})}, \qquad (8)$$

where the $\pm\mathbf{M}$ states are $\mathcal{T}$-related, and $I^\sigma(+\mathbf{M})$ is the SHG intensity generated by the $+\mathbf{M}$ magnetic order. The range of $\eta_{\mathcal{T}}^\sigma$ is $[-1,1]$ and $\eta_{\mathcal{T}}^\sigma = \pm 1$ represents the situation in which an incident CPL with helicity σ can only generate SH light in the $\pm\mathbf{M}$ magnetic states and is completely blocked in the opposite magnetic state. According to Eq. (6), the reversal of helicity and the reversal of magnetization are equivalent, and therefore the change of intensity under $\mathcal{T}$ operation can also be reproduced by changing the helicity of CPL at a fixed magnetization, i.e., $\eta_{\mathcal{T}}^+ = \eta_h^{+\mathbf{M}}$.

The expression of the NLMO intensity asymmetry in our case is (derivation is in Supplementary Note 2B)

$$\eta_{\mathcal{T}}^\pm = \mp \sin 2\delta \sin \Delta\varphi. \qquad (9)$$

As long as $\Delta\varphi \neq n\pi$, the NLMO intensity asymmetry is always nonzero, and the intensity of the SH light is always magnetization-dependent. In general, the maximum $|\eta_{\mathcal{T}}^\pm| = 1$ requires

$$\begin{cases} |\chi^{111}| = |\chi^{222}|, \\ \Delta\varphi = \pm\pi/2, \end{cases} \qquad (10)$$

and we denoted the corresponding frequency as the CPL characteristic frequency ω_{CPL}. This condition is also graphically shown in the complex plane in Supplementary Fig. 1. It is worth noting that the ω_{CPL} is just where the $\theta_{\mathcal{T}}$ for LPL is ill-defined.

We numerically traced the ω-dependence of $\eta_{\mathcal{T}}^+(2\omega)$ in the three representative materials in Fig. 3c. Again, two CrI$_3$-based materials can achieve large $\eta_{\mathcal{T}}^+$ including ± 1 at several frequencies while $|\eta_{\mathcal{T}}^+|$ is always below 0.4 in ML H-VSe$_2$. This contrast is another feature stemming from their distinct ratio of $|\chi_N|$ and $|\chi_M|$. We take ML Cr$_2$I$_3$Br$_3$ as an example to illustrate the intensity change of SH light under $\mathcal{T}$ operation for σ^+ CPL in Fig. 3d. (The CPL SHG intensity of ABA-AFM CrI$_3$ and ML H-VSe$_2$ are shown in Supplementary Figs. 4 and 8). The vertical dash line in Fig. 3d highlights one of the frequencies ω_{CPL} at which the intensity of SHG changes between a considerable value and zero under $\mathcal{T}$ operation. The upper (σ^+) and lower (σ^-) panels of Fig. 3d look exactly the same, except the line colors are swapped, which reflects the equivalence of helicity and magnetization reversal. Other than that, the difference in the red (blue) line between the upper and lower panels in Fig. 3d also indicates that this material exhibits a 100% SHG-CD effect at ω_{CPL}.

The giant NLMO effects discovered in CrI$_3$-based materials enabled them to be used as magnetic-field-controlled atomically thin optical devices, as illustrated in Fig. 3e. Utilizing incident light at frequencies ω'_{LPL}, they can serve as optical polarization switchers for LPL as they can rotate the
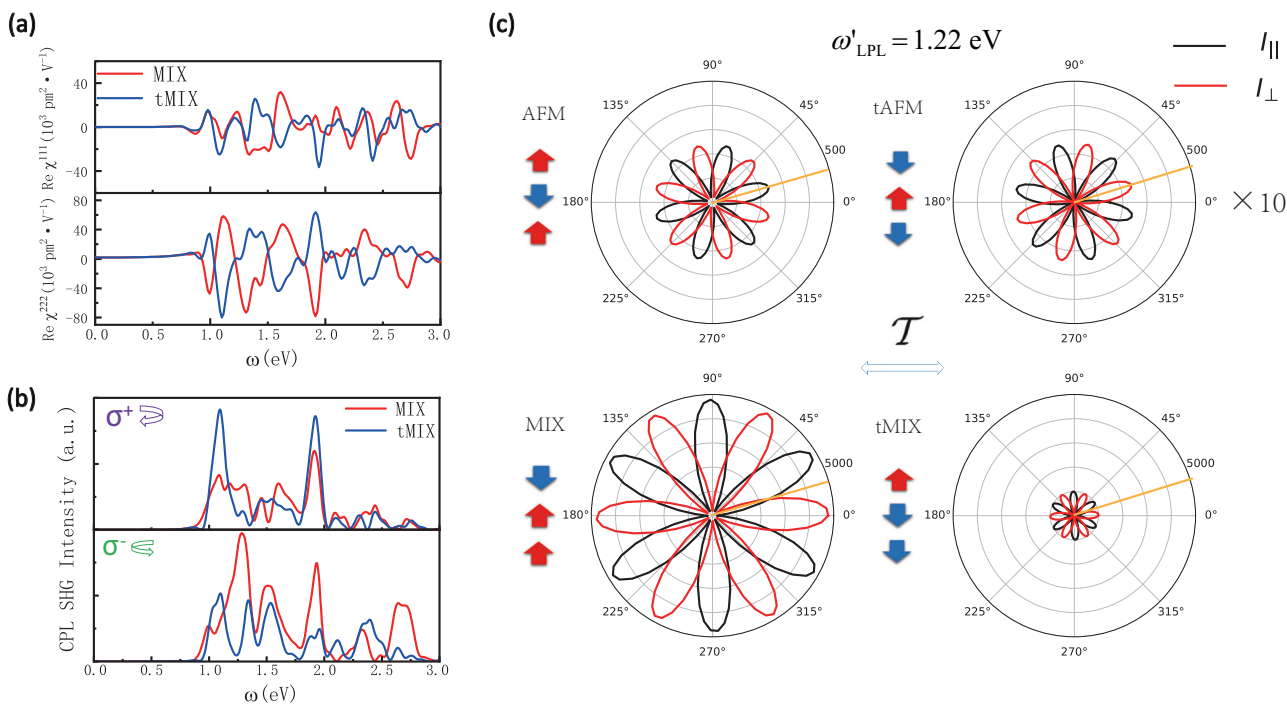
Fig. 4 | SHG susceptibility, CPL SHG intensity and polarization-resolved SHG for ABA-MIX CrI$_3$. a Real parts of SHG susceptibility tensor components of ABA-MIX CrI$_3$. Red and blue lines represent results for MIX($\uparrow\uparrow\downarrow$) and tMIX($\downarrow\downarrow\uparrow$) magnetic orders, respectively. **b** SHG intensity of MIX and tMIX magnetic orders of ABA-MIX CrI$_3$ under CPL illumination. The upper and lower panels are for incident helicity σ^+ and σ^-. The difference between the red and blue curves in each panel reflects the $\eta_{\mathcal{T}}$. For a particular magnetic order, the difference between the upper and lower panels reflects the magnitude of SHG-CD. **c** Polarization-resolved SHG of AFM, tAFM, MIX, and tMIX magnetic orders at one of the LPL frequency $\omega'_{\text{LPL}} = 1.22$ eV of ABA-AFM CrI$_3$. The red/blue arrow represents the magnetic moment in each CrI$_3$ layer.

polarization of SH light by nearly $\pi/2$. At the incident frequency ω_{CPL}, they are ideal magneto-optical switches for CPL due to their large $\eta_{\mathcal{T}}$. In addition, even without an external magnetic field, due to their large SHG-CD effects, they can serve as optical filters for CPL with a particular helicity.

It is worth noting that the above-discussed NLMO and SHG-CD effects are analyzed based on the nonlinear polarization $\mathbf{P}(2\omega)$ generated in materials, and the intensity of radiation is estimated by $I(2\omega) \propto |\mathbf{P}(2\omega)|^2$, which is not specific for the reflected or the transmitted SH light. The exact value of reflected and transmitted SH light can be obtained by solving Maxwell equations with corresponding boundary conditions[47]. Although the SH light in reflection or transmission may have different intensities, the above-discussed NLMO and SHG-CD effects persist.

The materials we investigated so far have several particular symmetry features. In general, NLMO effects are highly sensitive to changes in magnetic orders and can be used as a powerful tool to distinguish subtle magnetic states. As an example, we considered a different magnetic order $\uparrow\uparrow\downarrow$ for ABA stacking trilayer CrI$_3$, which we denoted as the MIX state and its $\mathcal{T}$-pair state as tMIX. ABA-MIX CrI$_3$ and ABA-AFM CrI$_3$ have the same net magnetic moment and tensor components as Table 1 shows, and their linear optical responses are similar, as shown in Supplementary Note 4, which makes them difficult to be distinguished experimentally. However, in ABA-MIX CrI$_3$, each SHG tensor component contains both χ_{N} and χ_{M} and does not have a definite parity under $\mathcal{T}$, as shown in Fig. 4a. As a result, for LPL, the polarization-resolved SHG shows both rotation and magnitude change under $\mathcal{T}$ operation as shown at the bottom two plots in Fig. 4c. For CPL, the equivalence between helicity and magnetization reversal, i.e., $\eta_h^{+\mathbf{M}} = \eta_{\mathcal{T}}^+$, is broken, as reflected by the remarkable difference between the upper and lower panels in Fig. 4b. Therefore, under the illumination of LPL (CPL) at ω_{LPL} (ω_{CPL}) for ABA-AFM CrI$_3$, we can observe notable differences between ABA-AFM CrI$_3$ and ABA-MIX CrI$_3$, as shown in Fig. 4c.

In addition to the detection of full ordered magnetic ground states, the NLMO effects can also distinguish the influence from spin fluctuation at

finite temperatures[22] and spin canting caused by an external field, as shown in Supplementary Fig. 6.

Controllable NLMO effects of representative 2D magnets

The giant NLMO effects manifest many intriguing applications as we have learned from the above results, a necessary condition to achieve those effects is to have comparable $|\chi_{\text{N}}|$ and $|\chi_{\text{M}}|$. However, in real materials, $|\chi_{\text{N}}|$ and $|\chi_{\text{M}}|$ may differ greatly, which results in negligible NLMO effects. In the following, taking ABA-AFM CrI$_3$ as a model system, we demonstrated several strategies to enhance NLMO effects, in which χ^{111} is the $\mathcal{T}$-odd term χ_{M} and χ^{222} is the $\mathcal{T}$-even term χ_{N} as summarized in Table 1.

The strength of interlayer interaction has a great impact on properties of multilayer magnets[37,48,49]; thus, we first investigated the influence of interlayer distance d in trilayer CrI$_3$, where d_0 is the interlayer distance of ABA-AFM CrI$_3$ at equilibrium. As shown in Fig. 5a, both $|\chi_{\text{M}}|$ and $|\chi_{\text{N}}|$ change with d, but $|\chi_{\text{N}}|$ is more sensitive to the variation of d. Therefore, a more comparable $|\chi_{\text{N}}|$ and $|\chi_{\text{M}}|$ can be realized by exerting hydrostatic pressure on multilayer CrI$_3$ along the z-axis in experiments, as shown in Fig. 5d.

Next, we investigated the influence of SOC on NLMO effects by artificially tuning the magnitude of SOC strength λ. As Fig. 5b shows, χ_{M} is sensitive to the change of λ while χ_{N} changes slightly. As $|\chi_{\text{M}}|$ is much larger than $|\chi_{\text{N}}|$ in ABA-AFM CrI$_3$, we replaced I by Br to reduce SOC and found ABA-AFM CrBr$_3$ possesses very comparable $|\chi_{\text{N}}|$ and $|\chi_{\text{M}}|$ in a broad frequency range, as shown in Fig. 5e.

Furthermore, we found stacking and magnetic orders can have synergistic effects on engineering the relative and absolute values of $|\chi_{\text{N}}|$ and $|\chi_{\text{M}}|$. As shown in Fig. 5c, in multilayer AB stacking AFM CrI$_3$, χ_{N} is forbidden in even-layer structures due to the presence of $\mathcal{PT}$ symmetry and remains almost the same in odd-layer structures, while χ_{M} increases with the layer number. The above observations can be simply understood as χ_{N} from each layer alternates the sign with similar magnitude, while χ_{M} from each layer has the same sign due to the $\mathcal{PT}$ symmetry between the A and the B
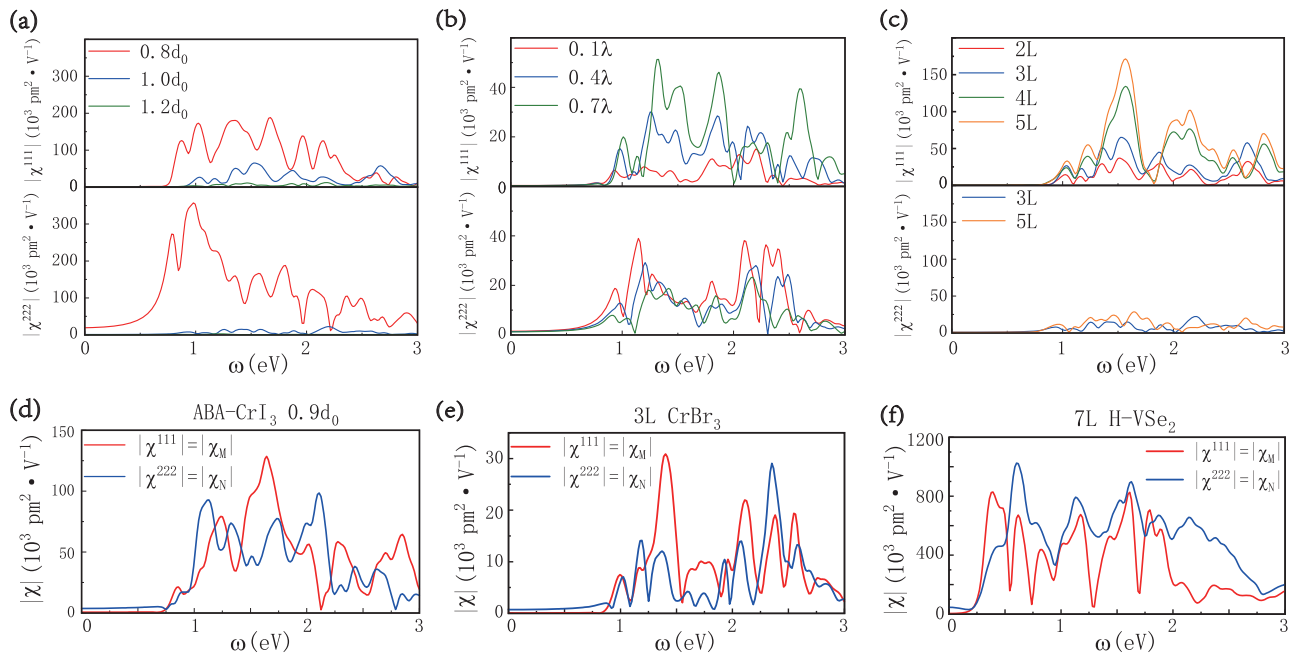
Fig. 5 | Design principles of NLMO effects. The influence of interlayer spacing (**a**), SOC (**b**), and layer number (**c**) to $|\chi^{111}|$ which is the $\mathcal{T}$-odd term χ_M and $|\chi^{222}|$ which is the $\mathcal{T}$-even term χ_N in ABA-AFM CrI$_3$ multilayers. The SHG tensor components of ABA-AFM CrI$_3$ with interlayer distance $0.9d_0$ (**d**), ABA-AFM CrBr$_3$ (**e**) and 7L H-VSe$_2$ (**f**). The $\mathcal{T}$-odd component $|\chi^{222}|$ in even-layer AFM CrI$_3$ is not shown.

layers[24]. Inspired by this, as $|\chi_M|$ is much smaller than $|\chi_N|$ in ML H-VSe$_2$, we calculated the SHG susceptibility of 7-layer (7L) AA'-AFM H-VSe$_2$, which also has $\mathcal{PT}$ symmetry between A and A' layers. As expected, the peak value of $|\chi_M|$ in 7L structure shown in Fig. 5f is almost 7 times that in ML H-VSe$_2$ (Fig. 2f) while its $|\chi_N|$ remains almost the same. $|\chi_N|$ and $|\chi_M|$ are comparable in 7L-AA' stacking H-VSe$_2$, indicating it can host giant NLMO effects. Similarly, by tuning the stacking sequence and magnetic order, we can achieve $\mathcal{P}$, $\mathcal{T}$ or neither symmetry between neighboring layers and can realize an arbitrary control of the relative and absolute value of $|\chi_N|$ and $|\chi_M|$ (Supplementary Fig. 9).

To summarize, the simultaneous breaking of $\mathcal{P}$, $\mathcal{T}$ and their joint symmetry allows NLMO effects with the electric-dipole origin. In several representative 2D magnets with similar symmetry, we investigated and demonstrated NLMO angle $\theta_{\mathcal{T}}$ under LPL, NLMO intensity asymmetry $\eta_{\mathcal{T}}$ and SHG-CD η_h under CPL. In particular, we discovered promising candidates with giant NLMO effects, including a near 90° polarization rotation and an on/off switching of certain helicity of SH light upon magnetization reversal, as well as ± 1 SHG-CD within a certain magnetic configuration. These giant NLMO effects in candidate 2D magnets can be used not only to design atomically thin NLMO devices such as optical polarization switchers, switches, and filters but also to detect subtle magnetic orders in multilayer magnets such as ABA CrI$_3$. We further derived that the comparable magnitude of $|\chi_N|$ and $|\chi_M|$ is indispensable to achieve giant NLMO effects. Lastly and most importantly, we found the interlayer distance, the magnitude of SOC, and the synergistic effect of stacking and magnetic orders could be used to control the relative and absolute magnitude of $|\chi_N|$ and $|\chi_M|$, which provides general design principles to achieve giant NLMO effects in 2D magnets. Our finding not only reveals several intriguing NLMO phenomena but also paves the way to achieve subtle magnetization detection, as well as giant and controllable NLMO effects in ultra-thin magneto-optical devices.

Methods
First-principles calculations
First-principles calculations were performed by Vienna *Abinitio* Simulation Package[50] with SOC included. The exchange-correlation function was parameterized in the Perdew–Burke–Ernzerhof form[51], and the projector augmented-wave potential[52] was used. For the $3d$ orbitals in magnetic ions

Cr and V, the Hubbard U of 3[37] and 1.16 eV[53] were used. For layered materials, we used DFT-D3 form van der Waals correction without damping[54]. The cut-off energy of plane waves was set to 450 and 500 eV for CrI$_3$-based materials and H-VSe$_2$-based materials, respectively. The convergence criterion of force was set to 10 and 1 meV Å^{-1} for CrI$_3$-based materials and H-VSe$_2$-based materials, respectively. Total energy is converged within 10^{-6} eV. k-point samplings of $13 \times 13 \times 1$ were used for CrI$_3$-based materials and $15 \times 15 \times 1$ for H-VSe$_2$-based materials. Vacuum thickness of about 20 Å was used in the calculations of 2D materials.

SHG calculations
After getting the converged electronic structures, we generated the maximally localized Wannier functions using Wannier90[55] to build the tight-binding Hamiltonian and calculate optical responses[34]. The $\mathcal{T}$ symmetry breaking is carefully treated in the calculations of SHG for magnets[35,56]. We obtained 56 maximally localized orbitals for each layer of CrI$_3$ or Cr$_2$I$_3$Br$_3$ and 22 for each layer of H-VSe$_2$. The broadening factor of the Dirac delta function is taken to be 0.05 eV. We found that $50 \times 50 \times 1$ and $150 \times 150 \times 1$ k-mesh samplings are enough for the converged SHG susceptibilities for CrI$_3$-based materials and H-VSe$_2$-based materials. The band gap of trilayer CrI$_3$ has been scissored to 1.5 eV in the calculation of SHG susceptibility[43].

Data availability
The data that support the findings of this study are available from the corresponding author upon request.

References
1. Sun, Z. et al. Giant nonreciprocal second-harmonic generation from antiferromagnetic bilayer CrI$_3$. *Nature* **572**, 497–501 (2019).
2. Zhang, Y. et al. Switchable magnetic bulk photovoltaic effect in the two-dimensional magnet CrI$_3$. *Nat. Commun.* **10**, 3783 (2019).
3. Wang, H. & Qian, X. Electrically and magnetically switchable nonlinear photocurrent in $\mathcal{PT}$-symmetric magnetic topological quantum materials. *npj Comput. Mater.* **6**, 199 (2020).

4. Fiebig, M. et al. Determination of the magnetic symmetry of hexagonal manganites by second harmonic generation. *Phys. Rev. Lett.* **84**, 5620–5623 (2000).

5. Fiebig, M., Pavlov, V. V. & Pisarev, R. V. Second-harmonic generation as a tool for studying electronic and magnetic structures of crystals: review. *J. Opt. Soc. Am. B* **22**, 96–118 (2005).

6. Pavlov, V. V., Pisarev, R. V., Kirilyuk, A. & Rasing, T. Observation of a transversal nonlinear magneto-optical effect in thin magnetic garnet films. *Phys. Rev. Lett.* **78**, 2004–2007 (1997).

7. Straub, M., Vollmer, R. & Kirschner, J. Surface magnetism of ultrathin γ-Fe films investigated by nonlinear magneto-optical Kerr effect. *Phys. Rev. Lett.* **77**, 743–746 (1996).

8. Kirilyuk, A. Nonlinear optics in application to magnetic surfaces and thin films. *J. Phys. D: Appl. Phys.* **35**, R189 (2002).

9. Huang, B. et al. Layer-dependent ferromagnetism in a van der Waals crystal down to the monolayer limit. *Nature* **546**, 270–273 (2017).

10. Mak, K. F., Shan, J. & Ralph, D. C. Probing and controlling magnetic states in 2D layered magnetic materials. *Nat. Rev. Phys.* **1**, 646–661 (2019).

11. Wu, S. et al. Extrinsic nonlinear Kerr rotation in topological materials under a magnetic field. *ACS Nano* **17**, 18905–18913 (2023).

12. Koopmans, B., Koerkamp, M. G., Rasing, T. & van den Berg, H. Observation of large Kerr angles in the nonlinear optical response from magnetic multilayers. *Phys. Rev. Lett.* **74**, 3692–3695 (1995).

13. Pershan, P. S. Nonlinear optical properties of solids: energy considerations. *Phys. Rev.* **130**, 919–929 (1963).

14. Pan, R.-P., Wei, H. D. & Shen, Y. R. Optical second-harmonic generation from magnetized surfaces. *Phys. Rev. B* **39**, 1229–1234 (1989).

15. Birss, R. R. *Symmetry and Magnetism* Vol. 3 (North-Holland Publishing Company, 1964).

16. Hübner, W. & Bennemann, K.-H. Nonlinear magneto-optical Kerr effect on a nickel surface. *Phys. Rev. B* **40**, 5973–5979 (1989).

17. Shen, Y.-R. *Principles of Nonlinear Optics* (Wiley-Interscience, New York, NY, USA, 1984).

18. Reif, J., Zink, J. C., Schneider, C.-M. & Kirschner, J. Effects of surface magnetism on optical second harmonic generation. *Phys. Rev. Lett.* **67**, 2878–2881 (1991).

19. Kirilyuk, A., Pavlov, V. V., Pisarev, R. V. & Rasing, T. Asymmetry of second harmonic generation in magnetic thin films under circular optical excitation. *Phys. Rev. B* **61**, R3796–R3799 (2000).

20. Gridnev, V. N., Pavlov, V. V., Pisarev, R. V., Kirilyuk, A. & Rasing, T. Second harmonic generation in anisotropic magnetic films. *Phys. Rev. B* **63**, 184407 (2001).

21. Train, C., Nuida, T., Gheorghe, R., Gruselle, M. & Ohkoshi, S. Large magnetization-induced second harmonic generation in an enantiopure chiral magnet. *J. Am. Chem. Soc.* **131**, 16838–16843 (2009).

22. Ogawa, Y. et al. Magnetization-induced second harmonic generation in a polar ferromagnet. *Phys. Rev. Lett.* **92**, 047401 (2004).

23. Toyoda, S. et al. Magnetic-field switching of second-harmonic generation in noncentrosymmetric magnet $Eu_2MnSi_2O_7$. *Phys. Rev. Mater.* **7**, 024403 (2023).

24. Li, Y. et al. Probing symmetry properties of few-layer MoS_2 and h-BN by optical second-harmonic generation. *Nano Lett.* **13**, 3329–3333 (2013).

25. Yin, X. et al. Edge nonlinear optics on a MoS_2 atomic monolayer. *Science* **344**, 488–490 (2014).

26. Abdelwahab, I. et al. Giant second-harmonic generation in ferroelectric $NbOI_2$. *Nat. Photonics* **16**, 644–650 (2022).

27. Guo, Q. et al. Ultrathin quantum light source with van der Waals $NbOCl_2$ crystal. *Nature* **613**, 53–59 (2023).

28. Kim, C.-J. et al. Stacking order dependent second harmonic generation and topological defects in h-BN bilayers. *Nano Lett.* **13**, 5660–5665 (2013).

29. Yao, K. et al. Enhanced tunable second harmonic generation from twistable interfaces and vertical superlattices in boron nitride homostructures. *Sci. Adv.* **7**, eabe8691 (2021).

30. Chu, H. et al. Linear magnetoelectric phase in ultrathin $MnPS_3$ probed by optical second harmonic generation. *Phys. Rev. Lett* **124**, 027601 (2020).

31. Lee, K. et al. Magnetic order and symmetry in the 2D semiconductor CrSBr. *Nano Lett.* **21**, 3511–3517 (2021).

32. Fonseca, J. et al. Anomalous second harmonic generation from atomically thin $MnBi_2Te_4$. *Nano Lett.* **22**, 10134–10139 (2022).

33. Song, Q. et al. Evidence for a single-layer van der Waals multiferroic. *Nature* **602**, 601–605 (2022).

34. Wang, C. et al. First-principles calculation of nonlinear optical responses by Wannier interpolation. *Phys. Rev. B* **96**, 115147 (2017).

35. Chen, H. et al. Basic formulation and first-principles implementation of nonlinear magneto-optical effects. *Phys. Rev. B* **105**, 075123 (2022).

36. McGuire, M. A., Dixit, H., Cooper, V. R. & Sales, B. C. Coupling of crystal structure and magnetism in the layered, ferromagnetic insulator CrI_3. *Chem. Mater.* **27**, 612–620 (2015).

37. Sivadas, N., Okamoto, S., Xu, X., Fennie, C. J. & Xiao, D. Stacking-dependent magnetism in bilayer CrI_3. *Nano Lett.* **18**, 7658–7664 (2018).

38. Jiang, P. et al. Stacking tunable interlayer magnetism in bilayer CrI_3. *Phys. Rev. B* **99**, 144401 (2019).

39. Jang, S. W., Jeong, M. Y., Yoon, H., Ryee, S. & Han, M. J. Microscopic understanding of magnetic interactions in bilayer CrI_3. *Phys. Rev. Mater.* **3**, 031001 (2019).

40. Soriano, D., Cardoso, C. & Fernández-Rossier, J. Interplay between interlayer exchange and stacking in CrI_3 bilayers. *Solid State Commun.* **299**, 113662 (2019).

41. Bonilla, M. et al. Strong room-temperature ferromagnetism in VSe_2 monolayers on van der waals substrates. *Nat. Nanotechnol.* **13**, 289–293 (2018).

42. X. Wang, et al. Ferromagnetism in 2D vanadium diselenide, *ACS nano* **15**, 16236 (2021).

43. Song, W., Fei, R., Zhu, L. & Yang, L. Nonreciprocal second-harmonic generation in few-layer chromium triiodide. *Phys. Rev. B* **102**, 045411 (2020).

44. Petralli-Mallow, T., Wong, T. M., Byers, J. D., Yee, H. I. & Hicks, J. M. Circular dichroism spectroscopy at interfaces: a surface second harmonic generation study. *J. Phys. Chem. C* **97**, 1383–1388 (1993).

45. Byers, J. D., Yee, H. I., Petralli-Mallow, T. & Hicks, J. M. Second-harmonic generation circular-dichroism spectroscopy from chiral monolayers. *Phys. Rev. B* **49**, 14643–14647 (1994).

46. Rodrigues, S. P., Lan, S., Kang, L., Cui, Y. & Cai, W. Nonlinear imaging and spectroscopy of chiral metamaterials. *Adv. Mater.* **26**, 6157–6162 (2014).

47. Zu, R. et al. Analytical and numerical modeling of optical second harmonic generation in anisotropic crystals using SHAARP package. *npj Comput. Mater.* **8**, 246 (2022).

48. Liu, X., Pyatakov, A. P. & Ren, W. Magnetoelectric coupling in multiferroic bilayer VS_2. *Phys. Rev. Lett.* **125**, 247601 (2020).

49. Jiang, X., Kang, L. & Huang, B. Role of interlayer coupling in second harmonic generation in bilayer transition metal dichalcogenides. *Phys. Rev. B* **105**, 045415 (2022).

50. Kresse, G. & Furthmüller, J. Efficient iterative schemes for ab initio total-energy calculations using a plane-wave basis set. *Phys. Rev. B* **54**, 11169–11186 (1996).

51. Perdew, J. P., Burke, K. & Ernzerhof, M. Generalized gradient approximation made simple. *Phys. Rev. Lett.* **77**, 3865–3868 (1996).

52. Kresse, G. & Joubert, D. From ultrasoft pseudopotentials to the projector augmented-wave method. *Phys. Rev. B* **59**, 1758–1775 (1999).

53. Gong, S.-J. et al. Electrically induced 2D half-metallic antiferromagnets and spin field effect transistors. *Proc. Natl Acad. Sci. USA* **115**, 8511–8516 (2018).

54. Grimme, S., Antony, J., Ehrlich, S. & Krieg, H. A consistent and accurate ab initio parametrization of density functional dispersion correction (DFT-D) for the 94 elements H-Pu. *J. Chem. Phys.* **132**, 154104 (2010).
55. Mostofi, A. A. et al. An updated version of Wannier90: a tool for obtaining maximally-localised Wannier functions. *Comput. Phys. Commun.* **185**, 2309–2310 (2014).
56. Kaplan, D. et al. Unifying semiclassics and quantum perturbation theory at nonlinear order. *SciPost Phys.* **14**, 082 (2023).

Author contributions

M.Y. conceived the project. D.W. carried out the DFT and NLMO calculations and analyzed the data. D.W. and M.Y. performed the analytical derivation of NLMO effects and analyzed the results. D.W. and M.Y. wrote the manuscript in consultation with all the authors. All authors discussed the results. M.Y. and Y.X. supervised the project.

Competing interests

The authors declare no competing interests.

Additional information

Supplementary information The online version contains supplementary material available at https://doi.org/10.1038/s41524-024-01266-x.

Correspondence and requests for materials should be addressed to Meng Ye or Yong Xu.

Reprints and permissions information is available at http://www.nature.com/reprints

Publisher's note Springer Nature remains neutral with regard to jurisdictional claims in published maps and institutional affiliations.